Immiscible displacement of oil by water in a microchannel: Asymmetric flow behavior and nonlinear stability analysis of core-annular flow

Hooman Foroughi,[*] Alireza Abbasi, Kausik S. Das, and Masahiro Kawaji[†]
Department of Chemical Engineering and Applied Chemistry, University of Toronto, Toronto, Ontario M5S 3E5
(Received 18 September 2011; revised manuscript received 10 January 2012; published 8 February 2012)

The immiscible displacement of oil by water in a circular microchannel was investigated. A fused silica microchannel with an inner diameter of 250 μm and a length of 7 cm was initially filled with a viscous silicone oil. Only water then was injected into the channel. We describe our flow observations based on the two-dimensional images captured in the middle of the channel. The water finger displaced the oil and left an oil film on the channel wall. While the oil was being displaced at the core, the flow resistance decreased, which resulted in increases in water flow rate and inertia. Eventually, the water finger reached the channel exit and formed a core-annular flow pattern. The wavelength of the waves formed at the oil-water interface also increased with the increase in inertia. The initially symmetric interfacial waves became asymmetric with time. Also, the water core shifted from the center of the channel and left a thinner oil film on one side of the microchannel. Under all flow rates tested in this study, as long as the water was continuously injected, the water core was stable and no breakup into droplets was observed. We also discuss the flow stability based on nonlinear and linear stability analyses performed on the core-annular flow. Compared to the linear analysis, which ignores the inertia effects, the nonlinear analysis, which includes the inertia effects, predicts longer interfacial wavelengths by a factor of $\frac{1}{\sqrt{1-\frac{a_o}{2}\left(\mathrm{We}_w+\mathrm{We}_o\frac{a_o^2}{1-a_o^2}\right)}}$ where We_w and We_o are the Weber numbers of the water and the oil phases, respectively, and a_o is the unperturbed water core radius made dimensionless by the channel radius.

DOI: 10.1103/PhysRevE.85.026309 PACS number(s): 47.15.Rq

I. INTRODUCTION

When a more viscous fluid is displaced by a less viscous fluid in a channel, the interface between the two fluids forms a finger. While the finger moves, it leaves a film of the more viscous fluid on the channel wall. This phenomenon is known as viscous fingering and was studied for the first time by Saffman and Taylor in a Hele-Shaw cell [1]. Viscous fingering frequently occurs in nature and in many engineering problems, including the immiscible displacement of oil in petroleum reservoirs. The past studies have usually been conducted in Hele-Shaw cells or in microchannels to approximate the flow in petroleum reservoirs [2,3].

Viscous fingering has been studied extensively mainly to predict the thickness of the film deposited on the channel wall. The phenomenon has been well documented in this regard and some correlations have been developed for film thickness prediction [4–8]. However, the thickness of the finger may not always match the predicted value and fluctuations in the finger width have been reported [9]. Perturbations at the interface were observed both in experiments [10–12] and in numerical simulations [13,14]. The stability of the viscous finger is also an important phenomenon to study. An unstable finger breaks up into droplets whereas a stable finger remains continuous and keeps growing [3].

In this work, we studied the displacement of viscous silicone oil by water in a microchannel. The focus of the previous studies has been more on the motion of a viscous finger front. In the present work, we continued the immiscible displacement experiments until the oil was completely displaced and the water occupied the entire channel. After the water finger had reached the channel outlet, the flow regime changed from fingering to core-annular flow where the water core was surrounded by an oil film. Although initially the flow regime was symmetric, the displacing water core shifted toward one side of a channel and asymmetric perturbations were observed at the interface with time. To the best of our knowledge, such flow behavior has not been reported in previous works. Under these experimental conditions, we have not observed any breakup and droplet formation during injection of water in the core. We will also discuss the stability of the displacing fluid based on nonlinear and linear stability analyses.

II. EXPERIMENTAL DETAILS

A. Materials

Silicone oil from Sigma Aldrich's 200 fluid series and deionized water were used as the working fluids. The air-oil surface tension and oil-water interfacial tension were 21 mN/m and 43 mN/m at 20 °C, respectively. The densities of the two fluids were close ($\frac{\rho_{\mathrm{water}}}{\rho_{\mathrm{oil}}}=1.03$ at 20 °C), while the oil was highly viscous compared to water ($\frac{\mu_{\mathrm{water}}}{\mu_{\mathrm{oil}}}=0.0012$ at 20 °C).

A circular fused silica microchannel (Polymicro Technologies) used in the experiments was 7.0 cm long and had an inner diameter of 250 μm. Both fluids were wetting and the contact angles for the oil-channel and water-channel were 25° and 30°, respectively. A schematic diagram of the apparatus is given in Fig. 1.

B. Experimental facility

The microchannel was first filled with silicone oil and then only water was injected into the microchannel to displace the

[*]hooman.foroughi@utoronto.ca
[†]kawaji@ecf.utoronto.ca

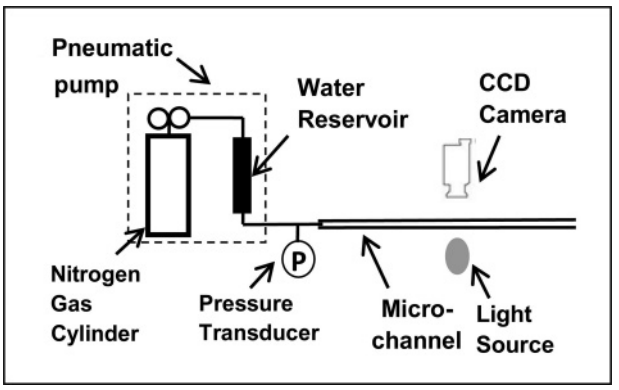

FIG. 1. A schematic of the experimental apparatus.

oil. As shown in Fig. 1, a pneumatic pump was used to inject water into a previously oil-saturated microchannel. The pump consisted of a nitrogen gas cylinder and a cylindrical stainless steel water reservoir. The reservoir was partially filled with water and was pressurized at the top by using a compressed nitrogen gas for water injection into the microchannel. A pressure transducer measured the pressure at the microchannel inlet and the channel outlet was open to the atmosphere.

A video camera was used to capture images of the water-silicone oil flow. To minimize the entrance and exit effects on the flow patterns observed, all images were captured in the middle of the channel at 140 diameters (3.5 cm) downstream of the channel inlet. Since a circular microchannel was used, optical correction was required to capture undistorted and clear images of the fluid interface near the channel wall. To this end, the microchannel was placed between two flat glass plates and the gap between the two plates was filled with the same silicone oil to best match the refractive index of the microchannel [15].

III. FLOW BEHAVIOR

A. Continuous water injection

Figure 2 shows the flow regimes observed in one experiment. All the images were captured in the middle of the channel at different times from the start of the water injection. The channel was first filled with oil [Fig. 2(a)], and then water was injected into the channel. The water finger displaced the oil at the center of the microchannel and left a continuous oil film on the channel wall [Fig. 2(b)].

Here, we define the initial capillary, Reynolds, and Weber numbers of the water phase based on the actual velocity of the water finger as follows:

$$\mathrm{Ca}_{wi} = \frac{\mu_w V_{wi}}{\sigma}, \tag{1}$$

$$\mathrm{Re}_{wi} = \frac{\rho_w V_{wi} D}{\mu_w}, \tag{2}$$

$$\mathrm{We}_{wi} = \frac{\rho_w V_{wi}^2 D}{\sigma}, \tag{3}$$

where μ_w is the viscosity of the water, V_{wi} is the velocity of the finger nose at the center of the channel, σ is the liquid-liquid interfacial tension, ρ_w is the density of the water, and D is the channel diameter. Table I gives the initial capillary, Reynolds, and Weber numbers of the water phase for the experiments

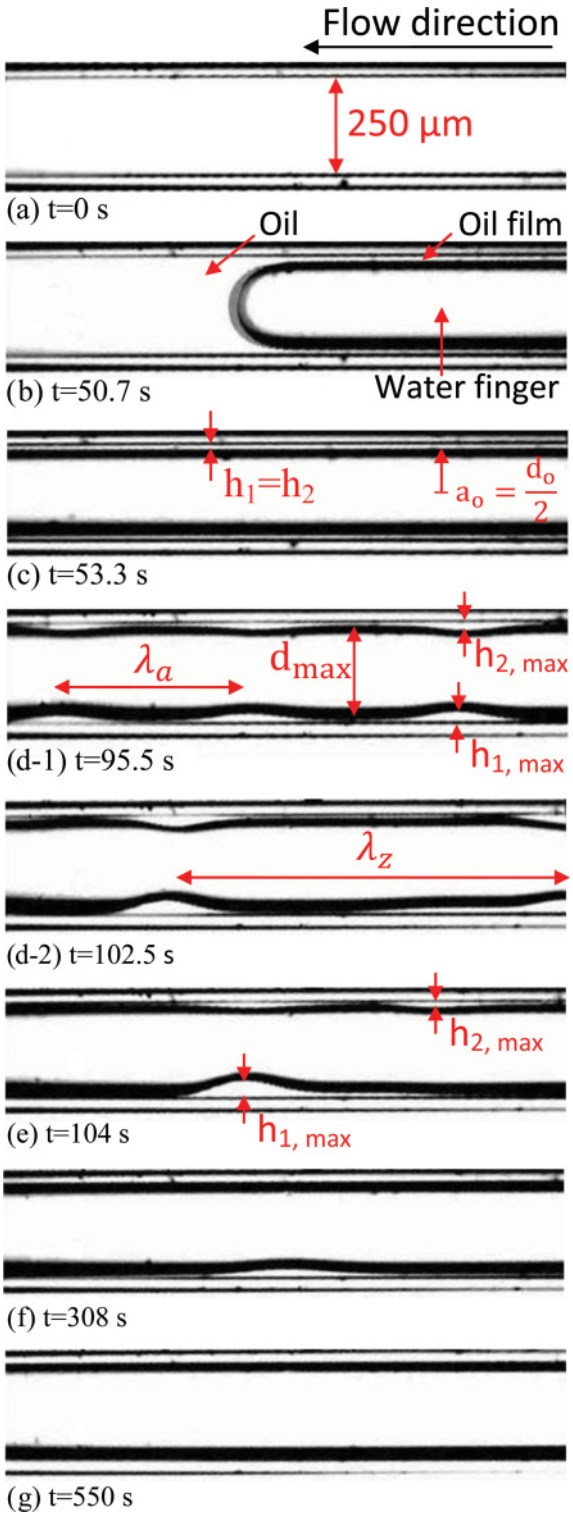

FIG. 2. (Color online) Flow patterns at $\mathrm{Ca}_{wi} = 4.8 \times 10^{-5}$ and $\overline{\mathrm{Ca}}_w = 9 \times 10^{-3}$ observed in the middle of the channel (top view) at different times from the start of the water injection: (a) the channel filled with stagnant oil; (b) the water finger displacing the oil at the core; (c) the oil film was left evenly on the channel wall and the oil-water interface was smooth; (d-1) symmetric perturbations formed at the interface; (d-2) the wavelength increased; (e) the water core shifted from the center and the flow became asymmetric; (f) the water core touched one side of the channel; (g) the oil was completely displaced.

TABLE I. Test conditions.

							Observations in the middle of the channel		
Ca_{wi}	Re_{wi}	We_{wi}	P_i (kPa)	$\overline{Ca}_w$	$\overline{Re}_w$	$\overline{We}_w$	Water finger first observed (s)	Start of perturbations (s)	Start of asymmetric behavior (s)
2.0×10^{-6}	0.02	4.1×10^{-8}	103	8.3×10^{-4}	8.3	0.007	714	Not observed	Not observed
3.6×10^{-5}	0.38	1.4×10^{-5}	112	5.4×10^{-3}	55	0.3	91	145	183
4.8×10^{-5}	0.48	2.3×10^{-5}	120	9.0×10^{-3}	91	0.8	50	82	103
1.7×10^{-4}	1.7	3.0×10^{-4}	163	3.4×10^{-2}	339	11.5	11.5	16	18
3.6×10^{-4}	3.6	1.3×10^{-3}	225	6.7×10^{-2}	672	45	5.2	6.8	7.1–10.8[a]
5.0×10^{-4}	5.1	2.6×10^{-3}	297	1.0×10^{-1}	1001	100	2.3	3.3	3.3–88[a]

[a]During these time periods, both symmetric and asymmetric perturbations were observed.

carried out in this study. The results presented in Fig. 2 are for $Ca_{wi} = 4.8 \times 10^{-5}$.

The unperturbed water core was thinner at higher water flow rates. This is consistent with the Bretherton scaling that predicts the oil film thickness to increase with the increased speed of the finger nose [4]. As shown in Fig. 3, the initial dimensionless radius of the water core, a_0, can be predicted by the semiempirical correlation of Eq. (4) suggested in Ref. [7] with 3% error. The radius of the water core was divided by the channel radius, R, to be made dimensionless,

$$a_o = 1 - \frac{1.34 \times ka_i^{2/3}}{1 + \left(2.5 \times 1.34 \times ka_i^{2/3}\right)}. \tag{4}$$

Here, ka_i is the capillary number of the form $\frac{\mu_o V_{wi}}{\sigma}$ where μ_o is the viscosity of the displaced fluid, i.e., oil. Under the conditions tested in this study, the dimensionless a_o varied between 0.7 and 1. The minimum film thickness we were able to determine from the images was 3 μm and films thinner than this limit were not visually observable. At the lowest flow rate tested in this work at $Ca_{wi} = 2.0 \times 10^{-6}$, the water core occupied the entire channel and the film left on the wall was too thin to be observed (Fig. 4). To reach such a low water flow rate, the nitrogen gas cylinder was removed from the pneumatic pump and, thus, the only pressure applied for water injection was hydrostatic, created by the height of the water column in the reservoir and the water flowed into the channel by gravity.

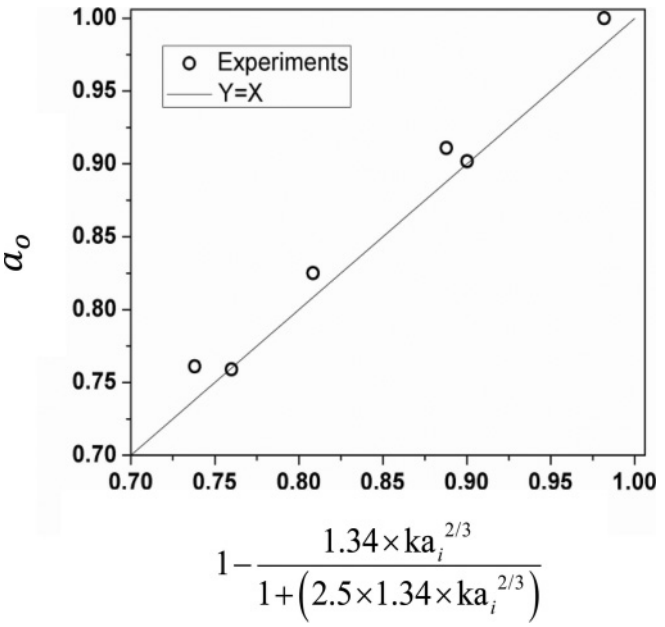

FIG. 3. Comparison of the measured initial water core radius with Eq. (4).

The resistance against the water flow was higher at the beginning of the experiments while the water displaced the oil at the center of the channel [Fig. 2(b)] which resulted in an initially low water velocity. This is primarily because the water had to displace a column of highly viscous oil out of the channel. The resistance against the flow was decreasing while the water finger was approaching the channel outlet. Figure 5 shows the time variation of the pressure at the channel inlet under different test conditions. The initial sharp decrease in the pressure drop, which was more noticeable at higher flow rates, was due to the oil displacement by the finger nose at the center of the channel. After the water finger reached the channel outlet and formed a fully core-annular flow, the pressure drop changed more smoothly with time. Since the resistance against the flow decreased, the water flow rate increased which resulted in higher capillary, Reynolds, and Weber numbers. Here, we define a second group of dimensionless numbers for the water phase based on the average superficial velocity of the water, $\bar{V}_w$, after the finger nose reached the channel exit:

$$\overline{Ca}_w = \frac{\mu_w \bar{V}_w}{\sigma}, \tag{5}$$

$$\overline{Re}_w = \frac{\rho_w \bar{V}_w D}{\mu_w}, \tag{6}$$

$$\overline{We}_w = \frac{\rho_w \bar{V}_w^2 D}{\sigma}, \tag{7}$$

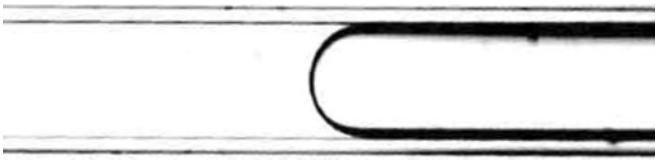

FIG. 4. The water finger at $Ca_{wi} = 2.0 \times 10^{-6}$ observed in the middle of the channel, at 714 s after the start of the water injection. The oil film on the channel wall is too thin to be observed.

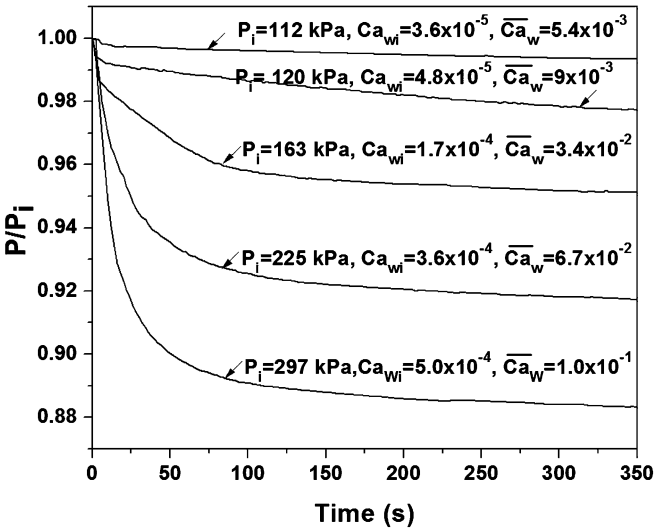

FIG. 5. Variation of the pressure at the channel inlet with time.

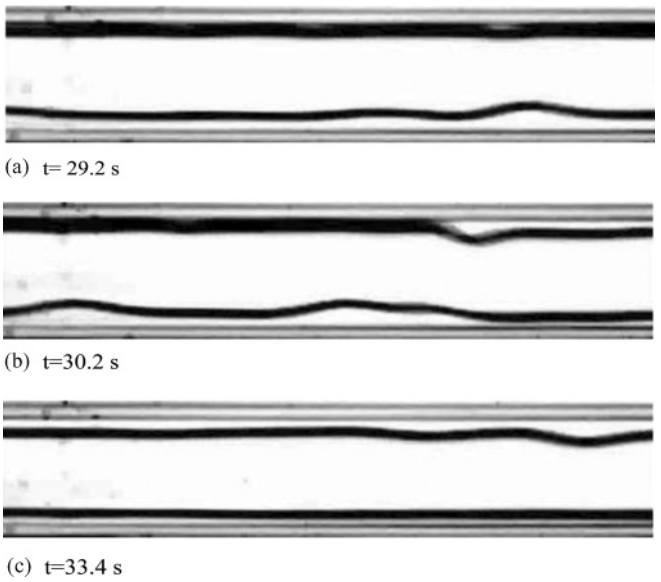

FIG. 6. The water core fluctuation between the sides of the channel at $\overline{\mathrm{Ca}}_w = 3.4 \times 10^{-2}$.

Assuming that the oil velocity is negligible compared to the water velocity, the average superficial velocity of the water can be calculated by dividing the mixture of the oil and water flow rate, Q_m, by the channel cross-sectional area:

$$\bar{V}_w = \frac{Q_m}{\frac{1}{4}\pi D^2}. \tag{8}$$

The results presented in Fig. 2 were at $\overline{\mathrm{Ca}}_w = 9.0 \times 10^{-3}$. As given in Table I, the values of $\overline{\mathrm{Ca}}_w$ are up to three orders of magnitude higher than those of Ca_{wi}.

At first, the water core was uniform in radius [Fig. 2(c)], but perturbations started to grow at the oil-water interface with time and formed travelling waves at the interface [Fig. 2(d)]. Generally, the formation of the interfacial perturbations took time. Depending on the channel length and the experimental condition, the interfacial waves could appear either during the immiscible displacement or in the core-annular flow regime. In this work, under the experimental conditions we tested with a 7-cm microchannel, the initial symmetric perturbations were observed in the core-annular flow regime.

The initiation and growth of perturbations took place earlier and faster, respectively, at higher water flow rates. Also, the speed at which the waves travelled along the oil-water interface increased with an increase in the water flow rate (Table II). The maximum wave speed we were able to measure by image analyses was 140 mm/s. Also, the maximum wavelength that could be measured was 5.6 mm ($\frac{\lambda}{R} = 45$). The wavelengths and wave speeds at $\overline{\mathrm{Ca}}_w = 6.7 \times 10^{-2}$ and $\overline{\mathrm{Ca}}_w = 10^{-1}$ were higher than this limit and are not reported in Table II.

In each experiment, the interfacial wavelength increased with time. The first wavelength, λ_a, and also the last symmetric wavelength observed at the interface λ_z, are shown in Figs. 2(d-1) and 2(d-2). The wave speed also increased with time (Table II). The increases in the wavelength and wave speed could be due to the increase in the water flow rate with time. This observation is in agreement with the results of the nonlinear stability analysis that will be presented later.

It should be noted that all descriptions of the flow pattern given are based on the two-dimensional images captured from the system. Although the initiation of disturbances was axially symmetric [Fig. 2(d)], these perturbations did not grow uniformly and the oil-water interface became asymmetric [Fig. 2(e)]. The time at which the system became asymmetric in each experiment is given in Table I. Also, the water core tended to shift toward one side of the channel and leave a thicker oil film on the other side. At low water flow rates ($\mathrm{Ca}_{wi} \leqslant 4.8 \times 10^{-5}$), the water core remained closer to one side, while at high flow ($\mathrm{Ca}_{wi} \geqslant 1.7 \times 10^{-4}$) rates, the core position fluctuated between the sides of the channel (Fig. 6).

TABLE II. Comparison of the initial (λ_a) and last symmetric (λ_z) wavelengths and wave speed with the results of the nonlinear (λ_{f1}) and linear (λ_{f2}) stability analyses.

				Initial wave formed				Last symmetric wave observed		
Ca_{wi}	$\overline{\mathrm{Ca}}_w$	$\frac{\lambda_z}{\lambda_a}$	Times (s)	Speed (m/s)	$\frac{\lambda_a}{\lambda_{f1}}$ [a]	$\frac{\lambda_a}{\lambda_{f2}}$	Times (s)	Speed (m/s)	$\frac{\lambda_z}{\lambda_{f1}}$ [b]	$\frac{\lambda_z}{\lambda_{f2}}$
0.03	4.5	1.09	162	9.4×10^{-5}	0.91	0.91	193	1.02×10^{-4}	0.93	1.02
0.04	7.5	1.84	95.5	2.5×10^{-4}	0.71	0.71	102	5.43×10^{-4}	1.13	1.31
0.14	28.2	2.37	16.7	3.4×10^{-3}	0.83	0.83	18.2	7.95×10^{-3}		3.60

[a] λ_{f1} is calculated with the initial velocities in the immiscible displacement flow regime.
[b] λ_{f1} is calculated with the values of a_0 given by Eq. (4) and velocities after the finger reached the channel exit.

In each experiment, we looked at the channel from a fixed angle either from the side or top. In all the experiments, as long as the oil film was thick enough to be observed, the flow became asymmetric with time. However, since simultaneous observations of flow from different angles could not be made, it is theoretically possible that the flow would have become asymmetric in the plane of our observation while it remained symmetric in another plane.

The asymmetric flow behavior was not due to gravity since the top and side views of the flow exhibited similar behavior. The low value of Bond number ($\mathrm{Bo} = 4 \times 10^{-4}$) defined below confirms that the gravity was negligible compared to other forces in the present system:

$$\mathrm{Bo} = \frac{\Delta\rho g D^2}{\sigma}, \tag{9}$$

where $\Delta\rho$ is the difference between the densities of the two fluids and g is the gravitational acceleration.

Once the water core became off-center, the drag forces were not uniform all around the interface and this could result in the asymmetric nature of the waves. Figure 7 shows how symmetric deformations at the interface were dragged and sheared at different rates and became asymmetric. Also, the interface may become wavy due to shear instability at high water flow rates ($\overline{\mathrm{Re}}_w \geqslant 95$) [15]. Once the velocity difference across the interface becomes sufficiently large, the interface can become unstable and wavy.

Understanding the asymmetric flow behavior of the water core requires further experimental and numerical investigations. However, the shift of the water core toward one side of the channel might be due to drag force minimization. As experimentally shown in Ref. [16], the drag force on a solid replica of a Taylor bubble that was placed in a liquid stream in a vertical tube decreased when the bubble was displaced from the tube axis. Similarly, in the current experiments, the shift of the water core from the center could decrease the overall drag force acting on the interface.

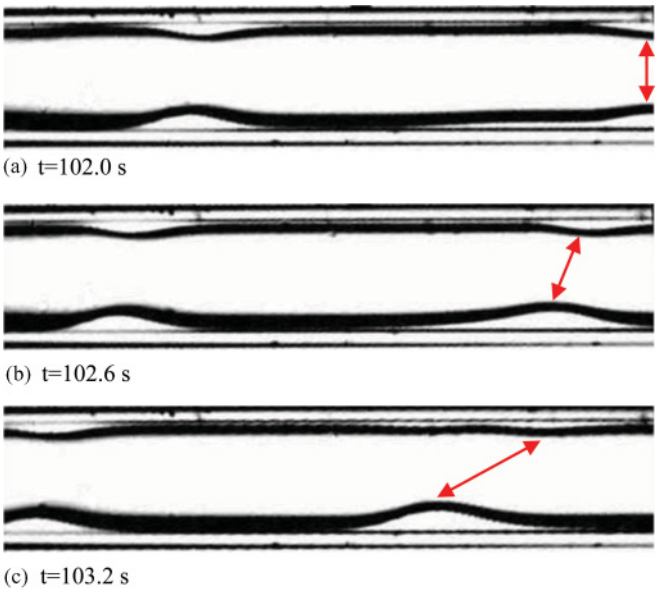

FIG. 7. (Color online) Flow patterns at $\mathrm{Ca}_{wi} = 4.8 \times 10^{-5}$ and $\overline{\mathrm{Ca}}_w = 9 \times 10^{-3}$, symmetric flow became asymmetric.

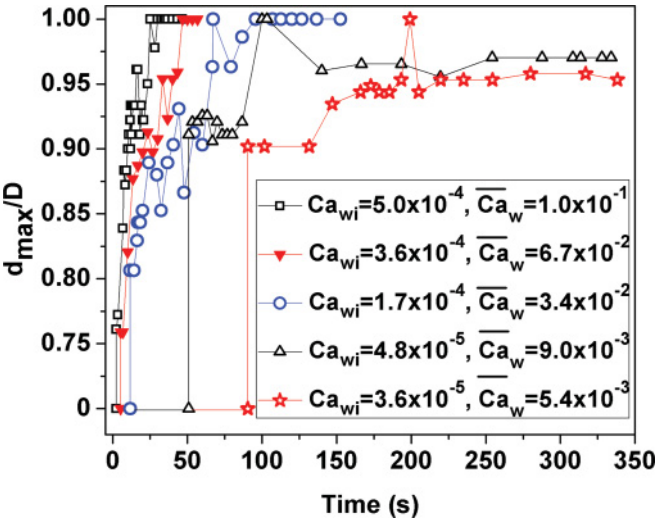

FIG. 8. (Color online) Variation of the maximum water core diameter with time.

The water core displaced the oil by pushing it and dragging it at the oil-water interface. The oil film thickness diminished and the water core diameter increased with time. Figure 8 shows how the maximum water core diameter, $d_{\max}$, changed with time under different test conditions [$d_{\max}$ is shown on Fig. 2(d-1) as an example]. At the beginning of the experiments when water was displacing a large oil volume in the core, the water finger was initially thicker at lower flow rates and the finger nose displaced the oil over a larger cross section. However, at higher flow rates the water finger displaced the oil over a smaller cross section but at a higher rate. Also, the drag force at the lateral oil-water interface was higher at higher flow rates and more oil was dragged at the interface. As shown in Fig. 8, the complete displacement of the oil occurred faster at the higher water flow rates.

To show how the oil film thickness changed with time, the maximum film thicknesses on both sides [$h_{1,\max}$ and $h_{2,\max}$ where $h_{1,\max} \geqslant h_{2,\max}$ as shown in Figs. 2(d-1) and 2(e)] were measured and the results are presented in Fig. 9. Initially, when the water core was at the center of the channel, $h_{1,\max}$ and $h_{2,\max}$ were equal. The maximum film thickness increased when the perturbations formed at the interface [compare Figs. 2(c) with 2(d)]. Both $h_{1,\max}$ and $h_{2,\max}$ then decreased while the oil was being dragged and pushed out by the water. Once the water core was shifted from the center, it left a thinner oil film on one side and the values of $h_{1,\max}$ and $h_{2,\max}$ began to differ [Fig. 2(e)]. As shown in Fig. 9, the difference was larger at lower water flow rates, implying that the eccentric flow behavior became more noticeable at lower water flow rates.

The wave height decreased faster on the thinner oil film [Fig. 2(e)] and the water core first touched the side of the channel where the film was thinner [Fig. 2(f)]. The wave height on the thicker oil film also decreased with time while the film was dragged. Finally, the water completely displaced the oil layer and occupied the entire microchannel [Fig. 2(g)].

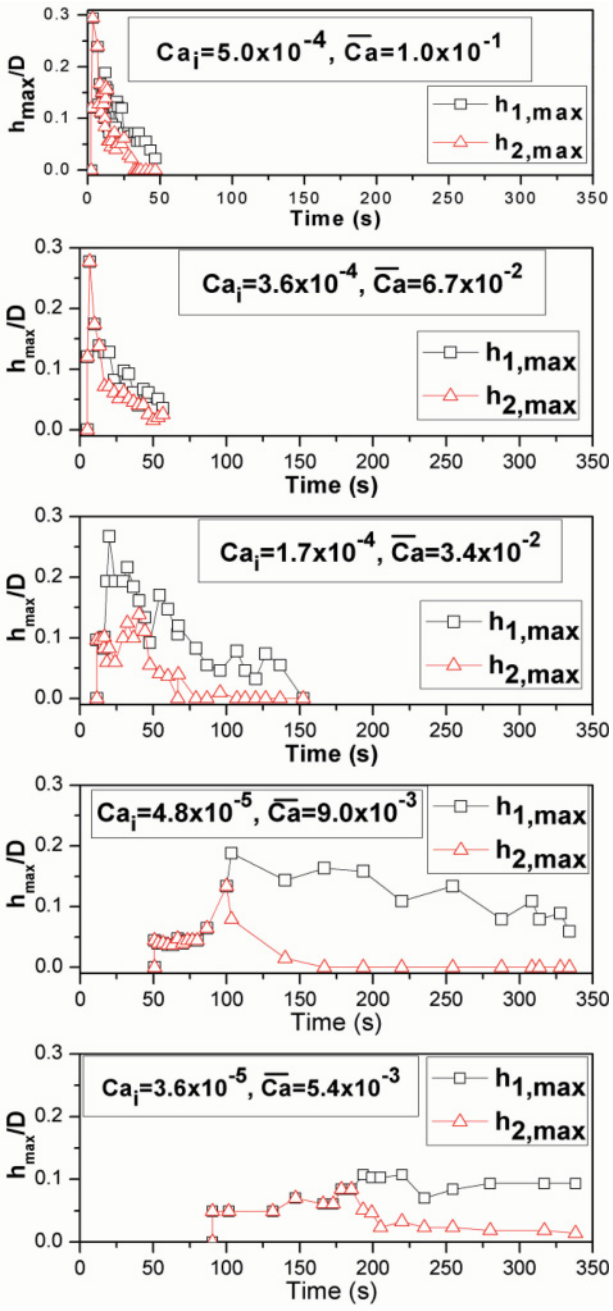

FIG. 9. (Color online) Variation of the maximum oil film thicknesses on opposite sides of the channel with time.

At all the flow rates tested in this study, as long as the water was continuously injected into the channel, the water core was always stable. No water core breakup was observed and the water always formed a continuous phase. However, in similar experiments carried out in Ref. [3] at $2.9 \times 10^{-6} \leqslant \mathrm{Ca}_{wi} \leqslant 4.1 \times 10^{-5}$ in a microchannel with an I.D. of 54 μm, the water core breakup always took place. Generally, the interfacial forces competed with inertia to make the water core unstable [15]. In core-annular flows, the interfacial tension forces tend to minimize the energy by breaking the water core into droplets and decreasing the interfacial area between the two fluids. These forces form symmetric interfacial deformations [Fig. 2(d-1)] and try to pinch the water core. On the other hand,

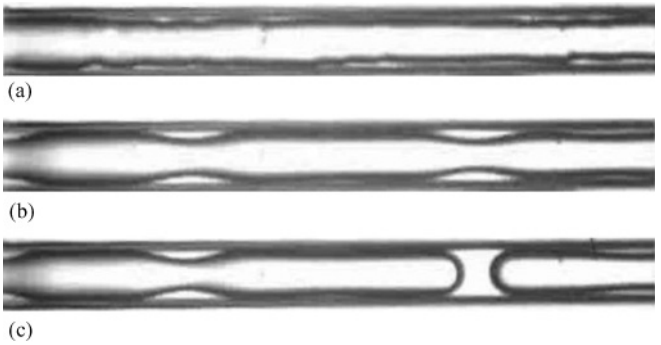

FIG. 10. Breakup of a stable water core into droplets after stopping the flow: (a) asymmetric continuous flow at $\overline{\mathrm{Ca}}_w = 3.2 \times 10^{-2}$; (b) formation of symmetric perturbations at 180 s after the flow was stopped; (c) breakup of a water core at 740 s after the flow was stopped.

the inertia tended to keep the water core continuous. In this work, while the oil was being displaced, the water flow rate and inertia and, consequently, the capillary number increased with time. When the perturbations appeared at the interface, the increase in the inertia was sufficiently large to keep the water core stable and also made the system asymmetric. This indicates that inertia can have an important effect on the flow stability and also morphology [17,18]. However, at low values of Ca_{wi} in Ref. [3], the interfacial forces were dominant and the water core breakup occurred.

B. Stopping the water injection

Generally, the system may remain stable while the water flow is maintained, but if the flow is stopped, the water core breakup can occur due to capillary instability [19]. In one experiment, after the observation of the asymmetric flow behavior in the system, we stopped the water flow rate. The symmetric perturbations appeared again and then the water core broke up, as shown in Fig. 10. This suggests that the asymmetric behavior is one of the characteristics of core-annular flow caused by inertia. Although the force due to interfacial tension was always present in the system, the inertia kept the water core continuous as previously reported in Ref. [15]. Once the water flow was stopped, however, there was no inertia to resist the interfacial tension force, and the symmetric deformations of the oil-water interface caused by interfacial tension finally broke up the water core into droplets. It is also noted that the oil film surrounding the water core needs to be sufficiently thick so the breakup of the water core can take place. We will discuss the stability of the system in the next section.

IV. STABILITY ANALYSIS

Here, we perform a nonlinear stability analysis on core-annular flow to predict the wavelength of perturbations formed at the oil-water interface. We use a similar approach as Ref. [20] to make the equations dimensionless. The following scales were used: channel radius, R, as the characteristic length, $W^* = \sqrt{\frac{\sigma}{\rho_o R}}$ as characteristic velocity, $\frac{R}{W^*}$ as characteristic time, and $P^* = \rho_o W^{*2}$ as characteristic pressure.

Generally, in the present notation, we use V as the velocity and U as the dimensionless velocity. Also, $\bar{V}$ and $\bar{U}$ are the average velocities. The dimensionless Navier-Stokes equations for both phases are

$$l\left(\frac{\partial U_w}{\partial t}+U_w\frac{\partial U_w}{\partial z}\right)=-\frac{dP_w}{dz}+\frac{m}{\mathrm{Re}^*}\frac{1}{r}\frac{\partial}{\partial r}\left(r\frac{\partial U_w}{\partial r}\right), \tag{10}$$

$$\frac{\partial U_o}{\partial t}+U_o\frac{\partial U_o}{\partial z}=-\frac{dP_o}{dz}+\frac{1}{\mathrm{Re}^*}\frac{1}{r}\frac{\partial}{\partial r}\left(r\frac{\partial U_o}{\partial r}\right), \tag{11}$$

where subscripts w and o represent water and oil, respectively, z is the dimensionless coordinate in the flow direction, U is the dimensionless z component of velocity, P is the dimensionless pressure, Re^* is the dimensionless Reynolds number of the form $\frac{\rho_o W^* R}{\mu_o}$, $l=\frac{\rho_w}{\rho_o}$ is the density ratio, $m=\frac{\mu_w}{\mu_o}$ is the viscosity ratio, t is the dimensionless time, and r is the dimensionless radius ($\mathrm{Re}^*=0.007$, $l=1.03$, $m=0.0012$ in this work).

The notation used in this analysis is for the case where the more viscous fluid is the outer fluid and the value of m is less than unity. If the inner fluid is more viscous, the subscripts w and o can be interchanged in Eqs. (10) and (11). Also, m, l, and Re^* can be replaced with $\hat{m}$, $\hat{l}$, and $\hat{\mathrm{Re}}^*$, where $\hat{m}=\frac{1}{m}$, $\hat{l}=\frac{1}{l}$, and $\hat{\mathrm{Re}}^*=\frac{\rho_w W^* R}{\mu_w}$ [20].

The velocity profiles of the two fluids in laminar core-annular flow are given by

$$U_w=\bar{U}_w\frac{(a^2-r^2)+m(1-a^2)}{\frac{a^2}{2}+m(1-a^2)},\quad 0\leqslant r\leqslant a, \tag{12}$$

$$U_o=\bar{U}_o\frac{r^2-1}{\frac{1}{2}(a^2-1)},\quad a\leqslant r\leqslant 1, \tag{13}$$

where $\bar{U}_w$ and $\bar{U}_o$ are the dimensionless cross section-averaged water and oil velocities, respectively, and a is the dimensionless radius of the water core, which could be a function of time. At the interface, the oil and water velocities are equal, i.e., $U_w=U_o$ at $r=a$. Since Eqs. (12) and (13) satisfy this condition, one can find the relation between the averaged oil and water velocities, $\bar{U}_w$ and $\bar{U}_o$.

We substitute Eqs. (12) and (13) into Eqs. (10) and (11), respectively, multiply by rdr, and then integrate Eq. (10) from $r=0$ to $r=a$ and Eq. (11) from $r=a$ to $r=1$. Integrating these equations allows us to work with the average velocities instead of velocity profiles [21]. This makes the analysis simpler since the oil and water velocities are functions of r, z, and t while the average velocities are only functions of z and t. The integrated Navier-Stokes equations are

$$l\frac{\partial}{\partial t}\left(\bar{U}_w\frac{a^2}{2}\right)+\frac{1}{2}l\frac{\partial}{\partial z}\left(\bar{U}_w^2\frac{a^2}{2}\right)=-\frac{dP_w}{dz}\left(\frac{a^2}{2}\right)+\frac{m}{\mathrm{Re}^*}\bar{U}_w\left(\frac{-2a^2}{m(1-a^2)+\frac{a^2}{2}}\right), \tag{14}$$

$$\frac{\partial}{\partial t}\left(\bar{U}_o\frac{1-a^2}{2}\right)+\frac{1}{2}\frac{\partial}{\partial z}\left(\bar{U}_o^2\frac{1-a^2}{2}\right)=-\frac{dP_o}{dz}\left(\frac{1-a^2}{2}\right)-\frac{4}{\mathrm{Re}^*}\bar{U}_o, \tag{15}$$

The mass conservation equations for the two fluids are

$$-\frac{d}{dz}(\bar{U}_w a^2)=\frac{d}{dt}(a^2), \tag{16}$$

$$\frac{d}{dz}\bar{U}_o(1-a^2)=\frac{d}{dt}(a^2), \tag{17}$$

Considering only the z-dependent perturbations, we use the perturbations of the form

$$a'=a_o\varepsilon\exp(\omega t+ikz), \tag{18}$$

$$\bar{U}_w'=\varepsilon\upsilon_w\exp(\omega t+ikz), \tag{19}$$

$$\bar{U}_o'=\varepsilon\upsilon_o\exp(\omega t+ikz), \tag{20}$$

where a_o is the radius of the unperturbed water core made dimensionless by the channel radius, ω is the dimensionless growth rate, $k=\frac{2\pi}{\lambda}$ is the dimensionless wave number, and λ is the dimensionless wavelength. The primes denote the perturbations. υ_w and υ_o can be found in terms of ω, a_o, and λ by inserting Eqs. (18)–(20) into Eqs. (16) and (17).

Also, the perturbed dimensionless normal stresses must balance at the interface,

$$\frac{\partial}{\partial z}(P_w'-P_o')=-\frac{1}{\mathrm{We}^*}\frac{\partial}{\partial z}\left(\frac{a'}{a_o^2}+\frac{\partial^2 a'}{\partial z^2}\right), \tag{21}$$

where We^* is the Weber number of the form $\frac{\rho_o W^{*^2} R}{\sigma}$ equal to 1. Equation (21) couples Eqs. (14) and (15) since it gives the relation between the perturbations in pressures of the two fluids. After introducing the perturbations into Eqs. (14), (15), and (21), Eqs. (14) and (15) can be combined into a single equation by using Eq. (21). Ignoring the second- and higher-order perturbation terms and also all the imaginary terms, this single equation results in the following dispersion relation for the growth rate:

$$A\omega^2+B\omega+C_1=0, \tag{22}$$

where the constants A, B, and C_1 are

$$A=2\left(l+\frac{a_o^2}{1-a_o^2}\right), \tag{23}$$

$$B=\frac{8}{\mathrm{Re}^*}\left[\frac{2a_o^2}{(1-a_o^2)^2}+\frac{m}{\left(m(1-a_o^2)+\frac{a_o^2}{2}\right)}\right], \tag{24}$$

$$C_1=\frac{a_o}{\mathrm{We}^*}k^4-\left(\frac{1}{a_o\mathrm{We}^*}-l\bar{U}_w^2-\frac{a_o^2}{1-a_o^2}\bar{U}_o^2\right)k^2, \tag{25}$$

or

$$C_1=\frac{1}{\mathrm{We}^*}\left[a_o k^4-\left(\frac{1}{a_o}-\frac{1}{2}\mathrm{We}_w-\frac{a_o^2}{2(1-a_o^2)}\mathrm{We}_o\right)k^2\right]. \tag{26}$$

Here, $\mathrm{We}^*=\frac{\rho_o W^{*^2} R}{\sigma}=1$ and $\mathrm{We}_w=\frac{\rho_w \overline{V}_w^2 D}{\sigma}$ and $\mathrm{We}_o=\frac{\rho_o \overline{V}_o^2 D}{\sigma}$ are the Weber numbers calculated with the properties and average velocities of water and oil, $\overline{V}_w$ and $\overline{V}_o$, respectively.

Between the two roots of Eq. (22), we choose the one that gives the asymptotic solution where ω goes to zero when k goes to zero. The solution to Eq. (22) is

$$\omega = -\frac{B}{2A} + \sqrt{\left(\frac{B}{2A}\right)^2 - \frac{C_1}{A}}. \tag{27}$$

The critical wavelength, λ_{c1}, at which the growth rate is zero and the fastest-growing wavelength, λ_{f1}, at which the growth rate is maximum can be given by Eqs. (28) and (29):

$$\lambda_{c1} = 2\pi a_o \left(\frac{1}{\sqrt{1 - \frac{a_o}{2}\left(\mathrm{We}_w + \mathrm{We}_o \frac{a_o^2}{1-a_o^2}\right)}} \right), \tag{28}$$

$$\lambda_{f1} = 2\sqrt{2}\pi a_o \left(\frac{1}{\sqrt{1 - \frac{a_o}{2}\left(\mathrm{We}_w + \mathrm{We}_o \frac{a_o^2}{1-a_o^2}\right)}} \right). \tag{29}$$

In the limit of low Re number, the Stokes approximation can be used to describe the system [22,23]. In Stokes equations the inertia terms, i.e., the second terms in Eqs. (10) and (11), are neglected and the analysis becomes linear. If the stability analysis is performed using the Stokes equations, the following dispersion relation is obtained for the core-annular flow:

$$A\omega^2 + B\omega + C_2 = 0, \tag{30}$$

where the constant C_2 is

$$C_2 = \frac{1}{\mathrm{We}^*}\left[a_o k^4 - \left(\frac{1}{a_o}\right)k^2\right]. \tag{31}$$

From Eq. (30), the following critical and also the fastest growing wavelengths can be found in the limit of low Re number where inertia is negligible:

$$\lambda_{c2} = 2\pi a_o \tag{32}$$

$$\lambda_{f2} = 2\sqrt{2}\pi a_o \tag{33}$$

The results of the linear analysis given by Eqs. (32) and (33) are in agreement with the results of the classical theory of the capillary instability of a cylindrical interface [24]. This critical wavelength is also the same as the one given in the analysis of viscous potential flow presented in Ref. [20]. Also, these results are in agreement with the results of previous analyses of core-annular flows in channels [25]. In Ref. [3], for the system of a thin film, it was shown that the fastest-growing wavelength would differ from Eq. (33) by a factor of $\frac{1}{\sqrt{1+C_V}}$, where C_V is the ratio of van der Waals forces to interfacial tension forces. Also, as experimentally shown in Ref. [12], when the effect of gravity becomes considerable, the fastest-growing wavelength would differ from Eq. (33) by a factor of $\frac{1}{\sqrt{1-2.5\mathrm{Bo}^2}}$.

Here we compare the results of the nonlinear stability analysis that considers the effect of inertia with those of the linear analysis in which the effect of inertia is neglected. In the linear analysis, the growth rate is a function of the unperturbed water core radius, Re number (Re^*), the density and viscosity ratios, and the wave number [Eq. (30)]. In the nonlinear analysis, the growth rate is a function of all these parameters as well as the oil and water Weber numbers [Eq. (22)]. Figure 11 compares the stability of the present system predicted by the two analyses. The growth rate predicted by the linear analysis,

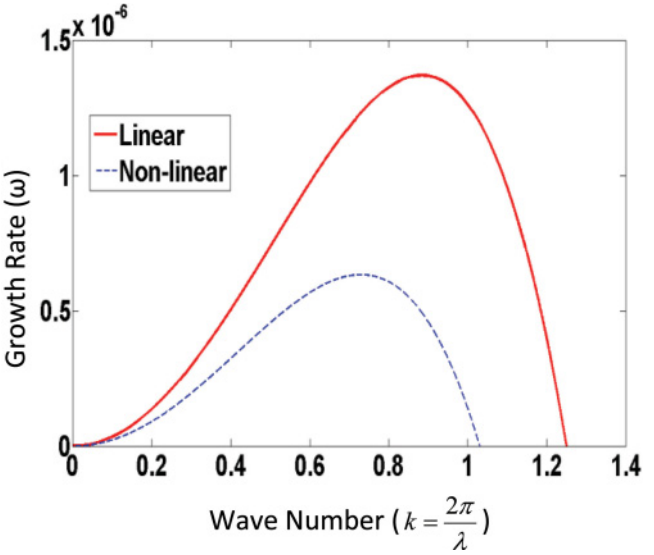

FIG. 11. (Color online) Dimensionless growth rate, ω, vs. dimensionless wave number, $k = \frac{2\pi}{\lambda}$, for $l = 1.03$, $a_o = 0.8$, $m = 0.0012$, $\mathrm{Re}^* = 0.007$, $\mathrm{We}_w = 0.8$, and $\mathrm{We}_o = 3 \times 10^{-5}$. The system predicted by the nonlinear analysis is more stable than the one predicted by the linear analysis.

in which the effect of inertia is neglected, is positive over a wider range of wave numbers. Also, for a given unstable wavelength, the growth rate of the linear analysis is higher than that of the nonlinear analysis. This indicates that considering the inertia effects makes the system more stable, which is in agreement with the experimental results. Generally, inertia tends to keep the water core continuous [15]. As mentioned earlier, under the experimental conditions tested in this study, as long as the water was injected into the channel, inertia kept the water core stable. The water core breakup took place only when the water flow was stopped.

Based on the results of the linear analysis [Eqs. (32) and (33)], the critical and the fastest-growing wavelengths are only a function of water core radius while in the nonlinear analysis [Eqs. (28) and (29)], these wavelengths are functions of the oil and water Weber numbers as well. The wavelengths predicted by the nonlinear analysis are higher by a factor of $\frac{1}{\sqrt{1-\frac{a_o}{2}\left(\mathrm{We}_w+\mathrm{We}_o\frac{a_o^2}{1-a_o^2}\right)}}$ compared to the values given by the linear analysis. This is in qualitative agreement with the experimental results where the interfacial wavelengths increased with an increase in inertia.

A quantitative comparison between the results of Eqs. (29) and (33) can also be made. Recalling that the relation between the average oil and water velocities is given by Eqs. (12) and (13) at the interface, two sets of Weber numbers for the oil and water phases were calculated for each experiment: the initial Weber numbers based on the velocity of the water finger in the midsection of the channel and also the Weber numbers based on the average water and oil velocities after the water finger reached the channel outlet. For the experimental conditions tested in this study, the factor, $\frac{1}{\sqrt{1-\frac{a_o}{2}\left(\mathrm{We}_w+\mathrm{We}_o\frac{a_o^2}{1-a_o^2}\right)}}$, in Eq. (29) calculated based on the initial values of the Weber numbers was very close to unity with a difference of less than

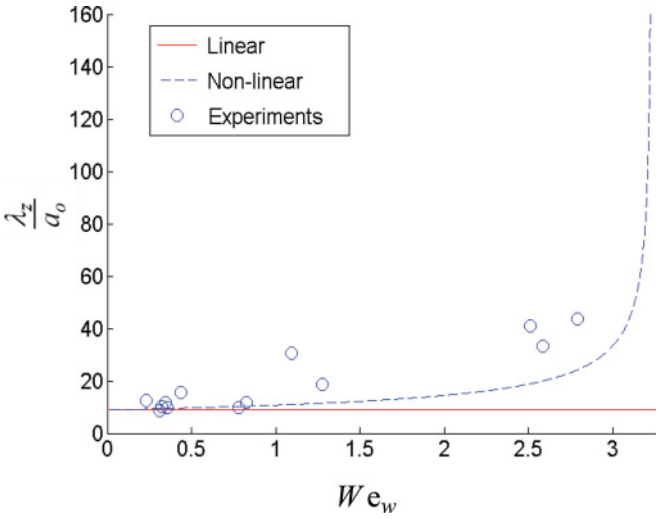

FIG. 12. (Color online) Variation of the fastest-growing wavelength with water Weber number; comparisons with the results of the nonlinear analysis, $\frac{\lambda_{f1}}{a_o}$ [Eq. (29)] and linear analysis, $\frac{\lambda_{f2}}{a_o}$ [Eq. (33)].

0.001. In other words, both analyses predict the same results in the limit of low initial Weber numbers. In Table III, we also compared the predictions of our nonlinear and linear analyses with the experimental results presented in Ref. [3] for the immiscible displacement of oil by water in a microchannel. In the limit of low velocities tested in Ref. [3] (Ca $<$ 0.022), both analyses predicted the same values of interfacial wavelengths with a maximum difference of 0.002%. Also, in Fig. 12, the results of the linear and nonlinear analyses for the system of oil and water used in this study are compared with the last symmetric wavelengths observed in the experiments. Additional experimental results were obtained in the limit of $We_w < 3$ for comparison in Fig. 12. As shown in this figure, the results of both analyses give the same values of wavelengths in the limit of low Weber numbers ($We_w < 0.25$). This indicates that ignoring the inertia terms is a valid assumption for systems with low Weber numbers.

Although the nonlinear and linear analyses provide similar results for the interfacial wavelengths in the limit of low flow rates, as given in Table II, the results of the two analyses differ when the wavelength in Eq. (29) is calculated with the Weber numbers based on the water and oil velocities after the water finger reached the channel outlet. In the case of linear analysis, the ratio of the last symmetric wavelengths in experiments to the one given by the analysis, i.e., $\frac{\lambda_z}{\lambda_{f2}}$, is more than unity, which indicates that the linear analysis underestimates the wavelength when the effect of inertia is not negligible. In the case of nonlinear analysis, as shown in Fig. 12, with an increase in the water velocity and, consequently, the Weber number, the nonlinear analysis predicts higher wavelengths compared to the linear analysis ($We_w > 0.25$). With a further increase in the Weber number ($We_w > 3$), the wavelength predicted by the nonlinear analysis approaches infinity which shows that averaging the inertial terms by integrating Eqs. (10) and (11) across the channel resulted in an overestimation of the fastest-growing wavelength at the interface in this limit.

TABLE III. Comparison between the results of the nonlinear (λ_{f1}) and linear stability (λ_{f2}) analyses with the experimental results ($\lambda_{\text{exp.}}$) presented in Ref. [3] for immiscible displacement of oil by water in a circular microchannel with a 54-μm inner diameter.

Ca	$\frac{\mu_w}{\mu_0}$	$\frac{\lambda_{\text{exp.}}}{\lambda_{f1}}$	$\frac{\lambda_{\text{exp.}}}{\lambda_{f2}}$
0.022	0.006	1.005	1.005
0.01	0.013	0.997	0.997
0.0024	0.053	1.083	1.083

V. CONCLUSION

The immiscible displacement of a viscous oil by water in a circular microchannel was investigated. We made flow pattern observations based on the two-dimensional images captured in the middle of the channel. First, a water finger flowed as a core with an initially low capillary number, Ca_i, and left an even oil film all around the channel wall. The oil-water interface was initially smooth, but symmetric perturbations formed at the lateral oil-water interface with time. While the oil was being displaced at the core and the water finger was approaching the channel outlet, the flow resistance decreased. This resulted in a decrease in the pressure drop inside the channel and an increase in the flow rate such that the capillary number increased from Ca_i to $\overline{Ca}$ by up to three orders of magnitude. Also, the interfacial wavelength and wave speed increased with the increase in the water flow rate. The water core then shifted from the center of the channel with time and the waves at the interface became asymmetric. In the range of the capillary number studied in this work ($8.3 \times 10^{-4} \leqslant \overline{Ca} \leqslant 10^{-1}$), water core breakup was not observed while water was continuously injected into the channel. However, when the water injection was stopped, the symmetric perturbations on the oil-water interface appeared again and broke up the water core into droplets.

We also performed nonlinear and linear stability analyses to predict the critical and fastest-growing wavelengths for a system of core annular flow. From these analyses, dispersion relations were derived analytically giving the growth rate of perturbations as a function of the viscosity and density ratios, Reynolds number (Re^*), the water core radius as well as the oil and water Weber numbers. The critical and the fastest-growing wavelengths predicted by the linear analysis are only a function of the water core radius while the wavelengths given by the nonlinear analysis are a function of the oil and water Weber numbers as well. The wavelengths predicted by the nonlinear analysis were higher than those predicted by the linear analysis. This is in qualitative agreement with the experimental results where the interfacial wavelength increased with an increase in inertia. A comparison between the results of the two analyses shows that the system becomes more stable when the effect of inertia is considered.

Since the stability of the system has been predicted to be a function of density and viscosity ratios, interfacial tension (the characteristic velocity and consequently the Re^* are functions of interfacial tension), and water core radius, a set of new experiments with systematic variations of fluid properties and channel radius can be performed and the results can be compared with those given by the stability analysis in future work.

ACKNOWLEDGMENT

The authors sincerely acknowledge the financial support from the Natural Sciences and Engineering Research Council of Canada, and support from a graduate fellowship for H. Foroughi from the University of Toronto. We also thank Professors Axel Guenther, Arun Ramchandran, Charles Ward, and Nasser Ashgriz at the University of Toronto for their helpful comments.

[1] P. G. Saffman and G. I. Taylor, Proc. R. Soc. London A **245**, 312 (1958).
[2] G. M. Homsy, Annu. Rev. Fluid Mech. **19**, 271 (1987).
[3] R. W. Aul and W. L. Olbricht, J. Fluid Mech. **215**, 585 (1990).
[4] F. P. Bretherton, J. Fluid Mech. **10**, 166 (1961).
[5] G. Taylor, J. Fluid Mech. **10**, 161 (1961).
[6] C.-W. Park and G. M. Homsy, J. Fluid Mech. **139**, 291 (1984).
[7] P. Aussillous and D. Quéré, Phys. Fluids. **12**, 2367 (2000).
[8] R. Krechetnikov and G. M. Homsy, Phys. Fluids. **17**, 102105 (2005).
[9] M. G. Moore, A. Juel, J. M. Burgess, W. D. McCormick, and H. L. Swinney, Phys. Rev. E **65**, 030601(R) (2002).
[10] K. V. McCloud and J. V. Maher, Phys. Rep. **260**, 139 (1995).
[11] M. Torralba, J. Ortín, A. Hernández-Machado, and E. Corvera Poiré, Phys. Rev. E **73**, 046302 (2006).
[12] V. Duclaux, C. Clanet, and D. Quere, J. Fluid Mech. **556**, 217 (2006).
[13] R. Ledesma-Aguilar, M. Quevedo-Reyes, E. Corvera Poiré, and A. Hernández-Machado, Phys. Rev. E **71**, 016312 (2005).
[14] M. Quevedo-Reyes, A. Hernández-Machado, and E. C. Poiré, Phys. Rev. E **73**, 066308 (2006).
[15] H. Foroughi and M. Kawaji, Int. J. Multiphase Flow **37**, 1147 (2011).
[16] E. T. Tudose and M. Kawaji, Chem. Eng. Sci. **54**, 5761 (1999).
[17] C. Chevalier, M. Amar, D. Bonn, and A. Lindner, J. Fluid Mech. **552**, 83 (2006).
[18] E. O. Dias and J. A. Miranda, Phys. Rev. E **83**, 066312 (2011).
[19] H. L. Goldsmith and S. G. Mason, J. Coll. Sci. **18**, 237 (1963).
[20] T. Funada and D. D. Joseph, Int. J. Multiphase Flow **28**, 1459 (2002).
[21] M. Johnson, R. D. Kamm, L. W. Ho, A. Shapiro, and T. J. Pedleyz, J. Fluid Mech. **233**, 141 (1991).
[22] I. G. Currie, in *Fundamental Mechanics of Fluids*, Chap. 8 (Marcel Dekker, New York, 2003), p. 288.
[23] P. Guillot, A. Colin, A. S. Utada and A. Ajdari, Phys. Rev. Lett. **99**, 104502 (2007).
[24] Lord Rayleigh, Proc. London Math. Soc. **s1-10**, 4 (1878).
[25] H. Hu and D. D. Joseph, J. Fluid Mech. **205**, 359 (1989).